

# Study of microstructure and mechanical property heterogeneity throughout the wall thickness of high strength aluminum alloy thick-wall pipe

Gaoyong Lin<sup>1,a)</sup>, Weiyuan Song<sup>1</sup>, Di Feng<sup>2</sup>, Kun Li<sup>1</sup>, Yongping Feng<sup>3</sup>, Jinxia Liu<sup>3</sup>

<sup>1</sup>School of Materials Science and Engineering, Central South University, Changsha, Hunan 410083, People's Republic of China; and Key Lab of Nonferrous Materials, Ministry of Education, Central South University, Changsha, Hunan 410083, People's Republic of China

<sup>2</sup>Department of Materials Science and Engineering, Jiangsu University of Science and Technology, Jiangsu 212003, People's Republic of China

<sup>3</sup>Fujian Xiangxin Shares Co., Ltd., Fuzhou 350000, People's Republic of China

<sup>a)</sup>Address all correspondence to this author. e-mail: mater218@163.com

Received: 2 January 2019; accepted: 25 March 2019

Differences in pipe wall microstructure at various positions throughout the wall thickness of high strength aluminum alloy thick-wall pipes produced by reverse hot extrusion were investigated. The microstructures of the inner wall (IW), outer wall (OW), and half wall (HW) were compared. Further, heterogeneity in the mechanical properties of the pipe throughout the wall thickness was also investigated. Results revealed that the volume fraction of precipitation was highest at the HW position because of the higher Zn and Mg contents. Further, approximately 26% of grains were recrystallized in the OW position due to the greater strain during extrusion, while the recrystallization fractions of the IW and HW positions were 13% and 21%, respectively. The effects of precipitation strengthening and deformation strengthening contribute to the highest ultimate tensile strength and Vickers hardness of the HW position, and to the higher elongation of the IW and OW positions.

## Introduction

Due to their low density, high strength, high fracture toughness, and excellent resistance to fatigue crack propagation after applicable deformation and heat treatment [1, 2], high strength aluminum alloys have attracted considerable attention in the aerospace industry. AlZnMgCu is an age-strengthening alloy; the main hardening phases of the alloy are the Guinier-Preston (GP) zone and the metastable  $\eta'$  (MgZn<sub>2</sub>) phase [3, 4, 5]. The Zn and Mg contents, the copper content segregation [6], and the aging temperature field gradient [7] play a crucial role in controlling the precipitation behavior and mechanical properties of high strength aluminum alloys. Further, Fe and Si impurities give rise to the formation of a coarse second phase, such as Al<sub>7</sub>Cu<sub>2</sub>Fe,  $\alpha$ -AlFeSi, and Mg<sub>2</sub>Si, in as-cast high strength aluminum alloys. The segregation of Fe and Si impurities also results in heterogenous coarse phase distribution [7, 8, 9]. Additionally, thermo-mechanical treatment leads to temperature gradient and strain gradient during deformation, which results in different dynamic softening behaviors and heterogeneity in the degree of recrystallization. A residual second phase

and high degree of recrystallization can degrade age hardenability, aid crack initiation and propagation, and cause heterogenous mechanical properties [7, 8, 9, 10, 11].

Generally, high strength aluminum alloys are produced in the form of a plate or extruded profile. Many previous studies of high strength aluminum alloys have focused on the heterogeneity of medium thick plates [9, 10, 11]. As mentioned above, there are many factors that may influence microstructure and heterogenous properties of high strength aluminum alloys, including the segregation of alloying elements in casting ingots, dissolution or precipitation of second phases during solution and aging, nonuniform deformation during hot-rolling, and so on [12, 13, 14, 15, 16]. Further, a study of the through-thickness texture gradient of a high strength 7055-T7751 plate showed that the  $\beta$  fiber texture was dominant in the center layer while shear textures were dominant near the surface [9]. The strength in the center layer is due to the high Taylor factor [17].

High strength aluminum alloy thick-wall pipes are widely used in the aerospace industry among others; they are primarily used for the load-carrying structure of an airplane,

for example, for the girder and junction [2]. In recent years, high strength aluminum alloy thick-wall pipes have been produced by reverse hot extrusion in order to reduce their deformation resistance [1]. Wei et al. [17] studied the heterogeneity in the texture of the through-wall thickness of 7050 aluminum alloy pipe using porthole die extrusion. Williams et al. [18] discussed the heterogeneity in the creep properties of the through-wall thickness of steel pipe. These studies [17, 18] indicated that the heterogeneity in the through-wall thickness properties of thick-wall pipes caused by microstructure differences reduced their effective load area and even resulted in premature failure. However, there have been almost no systematic studies on the microstructure and heterogenous properties of high strength aluminum alloy thick-wall pipes produced by reverse extrusion. In this research, the heterogeneity in the microstructure and mechanical properties throughout the wall thickness of aged high strength aluminum alloy thick-wall pipes prepared by reverse hot extrusion was investigated. The influence of the precipitated phase and the degree of recrystallization on heterogeneity of the through-thickness mechanical properties were discussed.

## Results

### Chemical composition

The chemical compositions of the inner wall (IW), half wall (HW), and outer wall (OW) were measured by a direct-reading spectrometer, and the deviation in the direct reading spectrometer is approximately 5%. Six points were selected for the drilling of metal powder samples to perform component detection in each region; the six points were randomly distributed over the area of the region under study. Table I and II show the chemical composition in the IW, HW, and OW regions of the extruded high strength alloy pipe and the primary high strength alloy hollow ingot, respectively. There is a clear difference in the content of alloying elements such as Zn, Cu, and Mg, and in the impurity elements Fe and Si, throughout the wall thickness due to macrosegregation. In particular, it should be noted that the Zn and Mg contents are highest in the HW region. It is known that the GP zone and  $\eta'$  phase are the main strengthening phases in AlZnMgCu alloys. Research [19] has revealed that the  $\eta'$  phase is a nonequilibrium phase and is semi-coherent with the Al matrix, consisting of a greater number of atomic layers (>6 layers) with high content of Zn and Mg elements. Therefore, it is of interest for the present paper to consider the effect of heterogeneity in Zn and Mg contents throughout the wall thickness of a high strength aluminum alloy extrusion pipe on the properties of this pipe.

**TABLE I:** Chemical composition at the HW, IW, and OW of the extruded high strength alloy pipe (wt%).<sup>a</sup>

Positions	Zn	Mg	Cu	Zr	Fe	Si	Mn	Ti	Al
IW	7.26	1.95	2.16	0.10	0.10	0.18	0.02	0.03	Bal
HW	7.65	2.09	2.35	0.10	0.12	0.07	0.02	0.02	Bal
OW	7.53	2.06	2.33	0.11	0.27	0.22	0.02	0.03	Bal

<sup>a</sup>The deviation of direct reading spectrometer is approximately 5%.

**TABLE II:** Chemical composition at the HW, IW, and OW of the primary high strength alloy hollow ingot (wt%).<sup>a</sup>

Positions	Zn	Mg	Cu	Zr	Fe	Si	Mn	Ti	Al
IW	7.33	1.98	2.18	0.11	0.13	0.20	0.03	0.02	Bal
HW	7.78	2.08	2.29	0.10	0.11	0.13	0.02	0.05	Bal
OW	7.52	2.12	2.30	0.11	0.28	0.23	0.05	0.04	Bal

<sup>a</sup>The deviation of direct reading spectrometer is approximately 5%.

### Mechanical properties

The ultimate tensile strength (UTS), yield strength (YS), elongation (El), and Vickers hardness of the specimens taken from the IW to the OW of the aged pipe are shown in Fig. 1. The Vickers hardness was measured on the cross section of the extruded pipe at sequential points every 2 mm, from the IW to the OW. The wall thickness of the tensile samples was 1.5 mm but there was wastage during machining. Therefore, tensile specimens were also taken along the radial direction (RD) every 2 mm.

It can be seen in Fig. 1 that there is significant heterogeneity in the mechanical properties of the alloy pipe. UTS, YS, and Vickers hardness showed similar trends; that is, UTS, YS, and Vickers hardness first increased and then decreased with increases in distance from the IW, while the trend in El was opposite. Therefore, the UTS, YS, and Vickers hardness at the HW were highest, while the El was lowest. The UTS, YS, Vickers hardness, and El values at the HW (10 mm) were 630.5 MPa, 613.21 MPa, 196.49 HV, and 8.5%, respectively. The El of the IW was 12.8%, which is higher than the other locations.

### Microstructural heterogeneity

#### Grain size and morphology

Cross-sectional metallographic photographs of the extruded high strength aluminum alloy pipe are shown in Fig. 2. Figures 2(b), 2(d), and 2(f) are the corresponding magnification images of Figs. 2(a), 2(c), and 2(e). It can be seen that the grains at the IW and OW are fine and have no obvious orientation, while the grains at the HW are coarse and distributed in a circumferential direction along the extruded pipe. During the extrusion process, the IW and OW of the pipe become deformed and the grains break, causing refined grains. The HW of the pipe is subjected to less deformation; thus, the

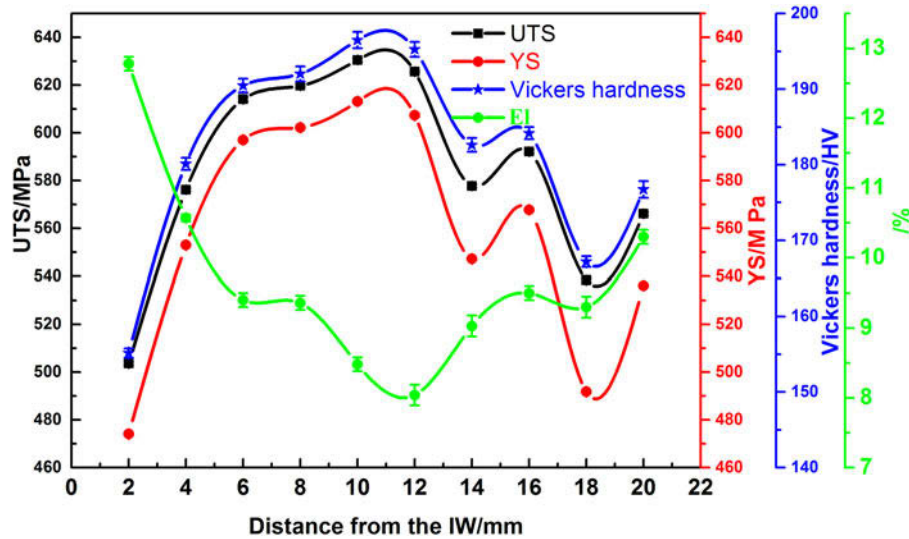


**Figure 1:** Mechanical properties of aged pipes from the IW to OW.

grains are coarse. Further, the grains at the HW of the pipe are subjected to extrusion tensile stress, resulting in preferred distribution of grains along the circumferential direction of the extruded pipe.

### Precipitated phase

The TEM bright field (BF) images along the  $[011]_{\alpha}$  zone axis inside the grains of the HW, IW, and OW samples are shown in Figs. 3(a), 3(c), and 3(e). The selected area diffraction patterns (SADPs) along the  $[001]_{\alpha}$  axes inside the grains are shown in Figs. 3(b), 3(d), and 3(f). It can be seen that the primary strong diffraction spots come from the  $\alpha$ -Al matrix. The small sharp diffraction spots at  $1/3\{220\}_{\alpha\text{-Al}}$  and  $2/3\{220\}_{\alpha\text{-Al}}$  in the  $[001]_{\alpha\text{-Al}}$  SAPDs, marked with white arrows, are from the metastable  $\eta'$  phase. The GPI zones are marked with yellow arrows. There are no obvious diffraction spots from other phases observed in the SAED. It can be confirmed that  $\eta'$  precipitation and GP zones are the main strengthening precipitates in high strength aged pipes. There were no significant differences in the diffraction patterns among the three regions of the pipe, but there were many diffuse streaks in the diffraction patterns of the IW.

A number of plate-like and needle-like  $\eta'$  precipitates in the matrix can be clearly observed in the corresponding BF images in Figs. 3(a), 3(c), and 3(e). The  $\eta'$  precipitates have an elongated direction perpendicular to  $g\{111\}_{\alpha\text{-Al}}$  [12]. It can be seen from Fig. 3 that the volume fraction and density of the precipitates are the largest in the HW, and that the values at the OW are slightly larger than those at the IW. The short axis size of the acicular precipitates in the HW is smaller than that in the OW and IW, and the radius of the elliptical or circular precipitates in the HW is smaller than that in the other two

regions. That is, the degree of coarsening of the precipitates in the HW is lower.

The high resolution transmission electron microscopy (HRTEM) micrographs obtained along the  $[110]_{\alpha\text{-Al}}$  zone axis in the Al matrix of aged 7055 alloy samples are shown in Fig. 4. The identification of different phases was roughly dependent on their sizes, which increased from  $\eta'$  (5–10 nm) to  $\eta$  precipitates (15–30 nm). Diffuse streaks and diffraction spots can be observed at the  $1/3$  and  $2/3\{220\}_{\alpha\text{-Al}}$  positions in the fast Fourier transformation (FFT) spectrum, indicating that  $\eta'$  precipitates have been formed.  $\eta'$  is coherent or semi-coherent with the Al matrix, consisting of more atomic layers ( $>6$  layers) [12]. The  $\eta'$  precipitations have an orientation relationship with the  $\alpha$ -Al matrix of the habit plane  $(0001)_{\eta'}$  parallel to  $\{111\}_{\alpha\text{-Al}}$  [20]. Due to the presence of four equivalent  $\{111\}_{\alpha\text{-Al}}$ , there are four equivalent orientations for  $\eta'$  precipitates in the  $\alpha$ -Al matrix. In Figs. 4(a), 4(b), and 4(d), elongated precipitates are two of the four  $\eta'$  variants, which are edge-on and marked with white arrows; the other two are observed to be tilted ellipsoid and are marked with blue arrows [12]. Differences in the types of precipitates at the HW, IW, and OW regions can be observed. According to the FFT and the size of the precipitates, it can be inferred that the precipitates at the IW and HW are mainly  $\eta'$  precipitations;  $\eta'$  is semi coherent with the Al matrix, but the size of the  $\eta'$  precipitations and the density varies greatly. The diameter of the tilted ellipsoid  $\eta'$  precipitations is about 8.8 nm, and the thickness of the marked elongated  $\eta'$  precipitates is about 6.7 nm; the length is about 12.5 nm at the IW. However, the diameter of the ellipsoid  $\eta'$  precipitations is 4–7 nm, and the marked elongated  $\eta'$  precipitates are 1.5 nm thick and 4–7 nm wide at the HW. Further, the size of the  $\eta'$  precipitations at the OW is slightly larger than

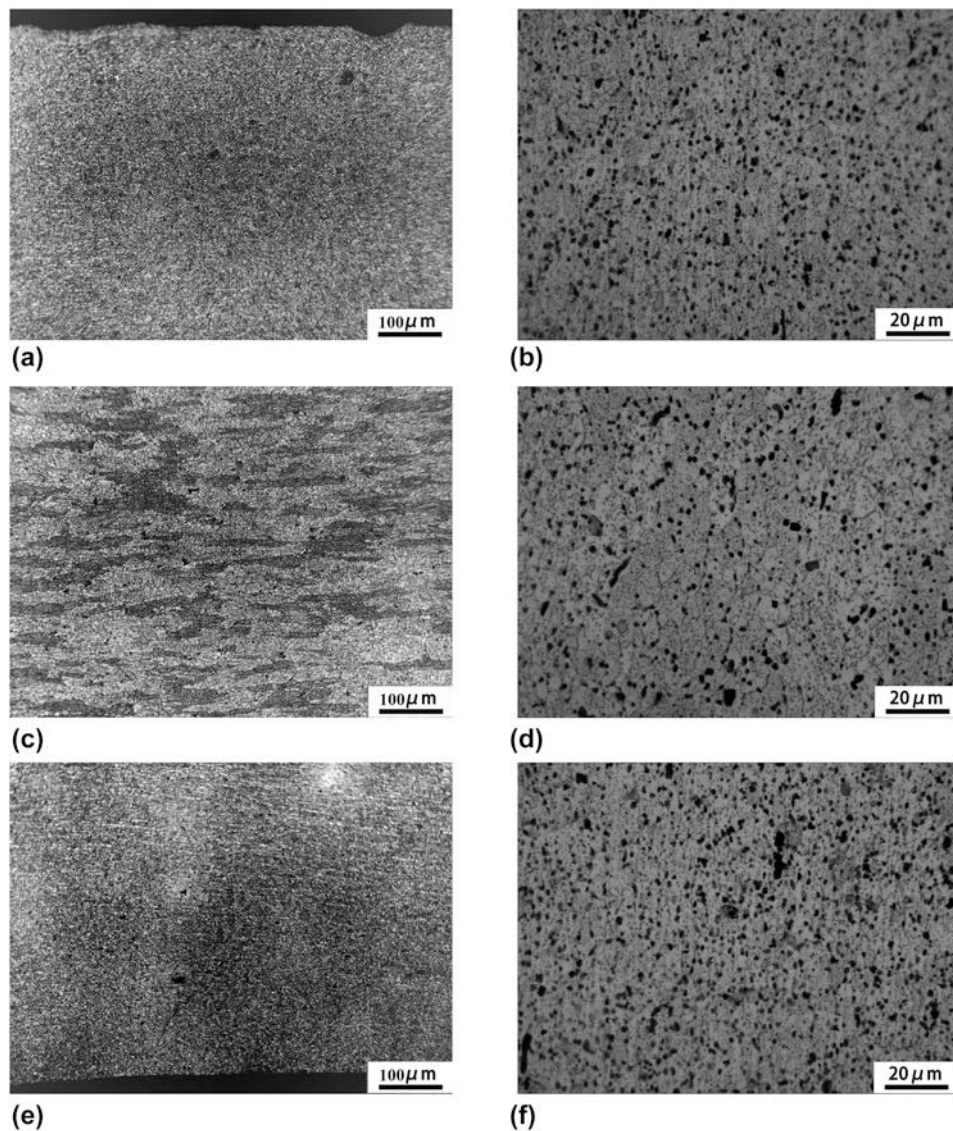


**Figure 2:** Cross-sectional metallographic photographs of extruded high strength pipe. (a) and (b) at the IW; (c) and (d) at the HW; (e) and (f) at the OW.

those at the HW.  $\eta$  precipitates that are formed by  $\eta'$  and are completely incompatible with the Al matrix are observed at the HW, with a length of 19.4 nm.

### Grain structure

The orientation imaging microscopy (OIM) images of the aged high strength alloy pipes are shown in Fig. 5. It can be seen that there are significantly grains orientation in all three regions of the pipe, and the grains are elongated along the extrusion direction. In Fig. 5, different colors represent different crystallographic orientations: blue, yellow, and red represent recrystallized grains, substructured grains, and deformed grain, respectively. Figure 5 shows a clear difference among the IW, HW, and OW regions. In particular, at the

OW, dynamic recovery occurred during the heat treatment, and as a result, about 50% of grains are substructured and 25% of grains are recrystallized. In contrast, around 50% of grains remain deformed at the HW, while nearly 20% of grains are recrystallized.

### Discussion

Transition phase  $\eta'$  precipitation is a kind of nonequilibrium precipitate, and it has a hexagonal structure with lattice constants as follows:  $a = 0.49$  nm,  $c = 1.43$  nm.  $\eta'$  precipitation is coherent or semi-coherent with the matrix and has a remarkable strengthening effect [5, 21], and it is the main strengthening phase of the aluminum alloy studied in this paper. The composition of the  $\eta'$  phase is MgZn, and it can be



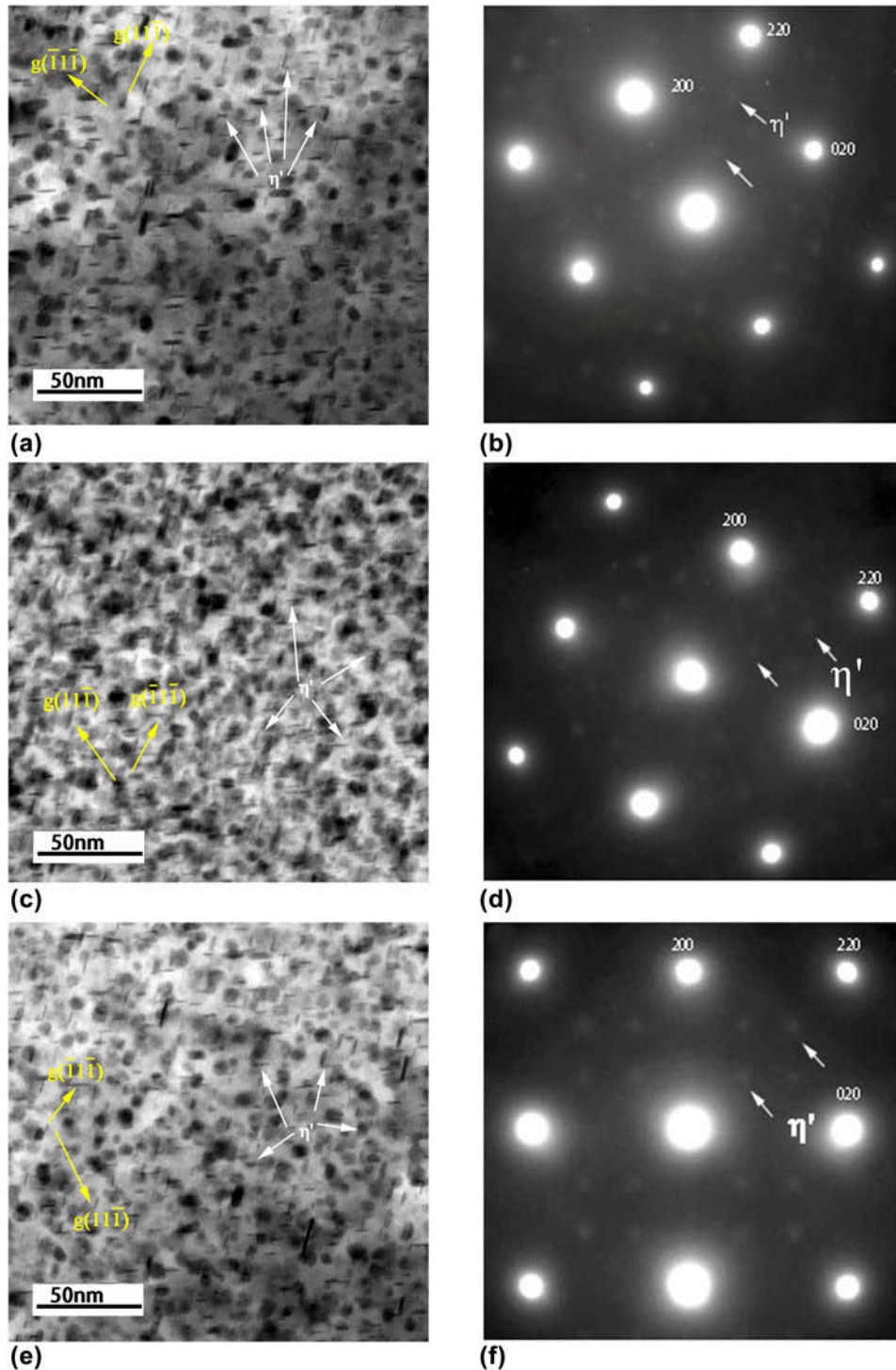


**Figure 3:** BF images and SAED of inner precipitates of aged high strength alloy samples. (a) and (b) at the IW; (c) and (d) at the HW; (e) and (f) at the OW.

precipitated directly from supersaturated solid solution. The density and phase size of  $\eta'$  precipitation are directly related to the chemical composition of the alloy, particularly the content of Zn, Mg, and Cu in the alloy. When the ratio of Zn/Mg in the alloy is larger than 2.2,  $\eta'$  phase will precipitate in the alloy.

Increasing the content of Zn and Mg in the alloy within the solution limit can increase the precipitation of  $\eta'$  phase in the alloy, thus greatly improving the strength and hardness of the alloy [12, 19]. As can be seen from Table I, the contents of Zn, Mg, and Cu at the IW, HW, and OW were different; thus,

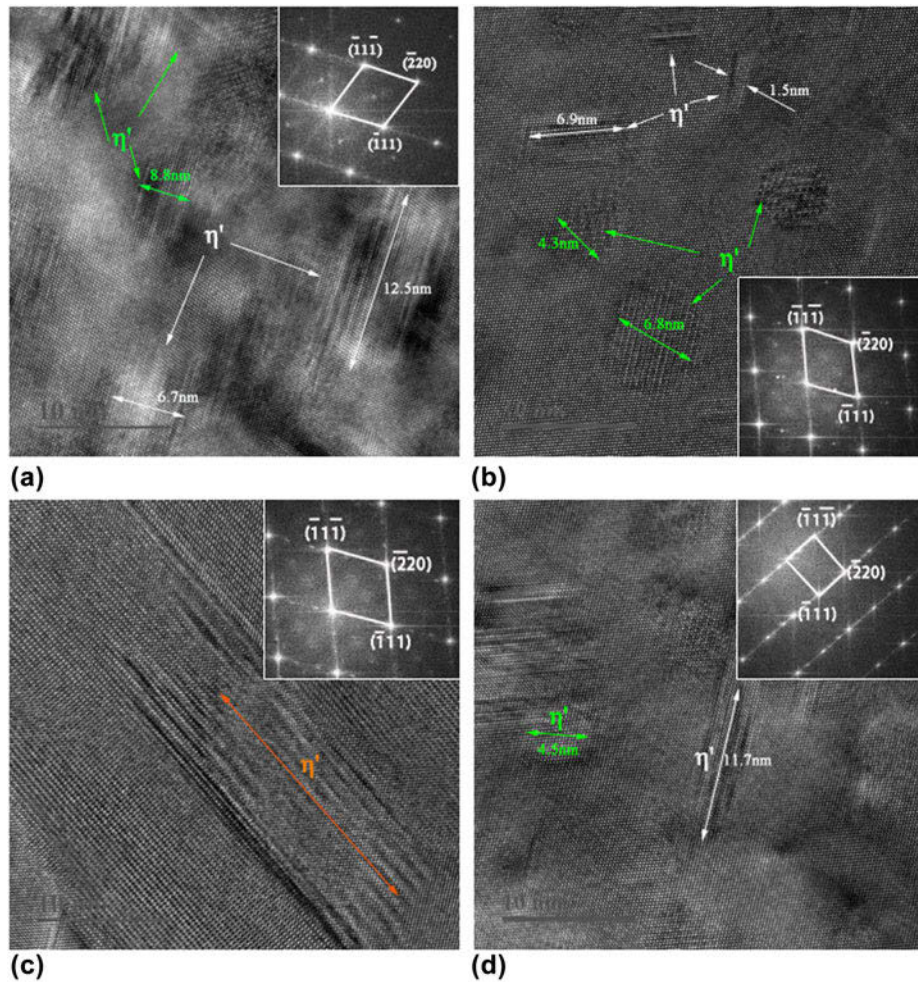


**Figure 4:** HRTEM micrographs obtained along the  $[110]_{\alpha-Al}$  zone axis in the Al matrix of aged 7055 alloy samples: (a) at the IW; (b) at the HW; (c) and (d) at the OW.

the precipitation of  $\eta'$  phase in the aluminum alloy in these regions is also different.

Cu elements can make the aging microstructure more uniform, improve its strength and plasticity, and increase stress corrosion resistance [22]. Cu can increase the degree of supersaturation of an alloy, accelerate the artificial aging process between 100 and 200 °C, promote the precipitation of  $\eta'$  phase, and expand the stable range of the  $\eta'$  phase. As shown in Table I, the content of Cu in the IW, HW, and OW of the aluminum alloy pipe was different, and the plasticity differed among these regions (Fig. 1). At the HW and OW, the content of Cu is higher and the plasticity is better than that at the OW. In order to reduce composition segregation in the pipe, the stirring speed during melting and the cooling speed of the ingot should be accelerated during the process of pipe ingot casting so as to ensure that the composition of the pipe is more uniform [23].

The volume fraction of recrystallization and the area volume fraction of the second phases of the IW, HW and

OW are shown in Fig. 6. It can be seen from Fig. 6 that a large number of fine dispersed second phases have been precipitated in the HW, owing to the high content of Al and Zn elements, and the area volume fraction is the largest at the HW. The content of Zn and Mg at the IW is the lowest and less  $\eta'$  phase is precipitated at the IW. The movement of the dislocations could be effectively blocked by the precipitates. Since the dislocations could pass  $\eta'$  phases by cutting through them, the strengthening effect can be expressed as the following [24]:

$$\Delta\sigma = c_1 f^m r^n \quad (1)$$

where  $c_1$ ,  $m$ , and  $n$  are the constants,  $f$  is the area volume fraction of the second phases, and  $r$  is the radius of the precipitation. It is clearly observed from Fig. 6 that the area volume fractions of the second phase ( $f$ ) of the IW, HW, and OW have a remarkable increasing trend, so the strength and hardness at the HW of the pipe is the highest, followed by the OW, and the IW is the lowest, as shown in Fig. 1.



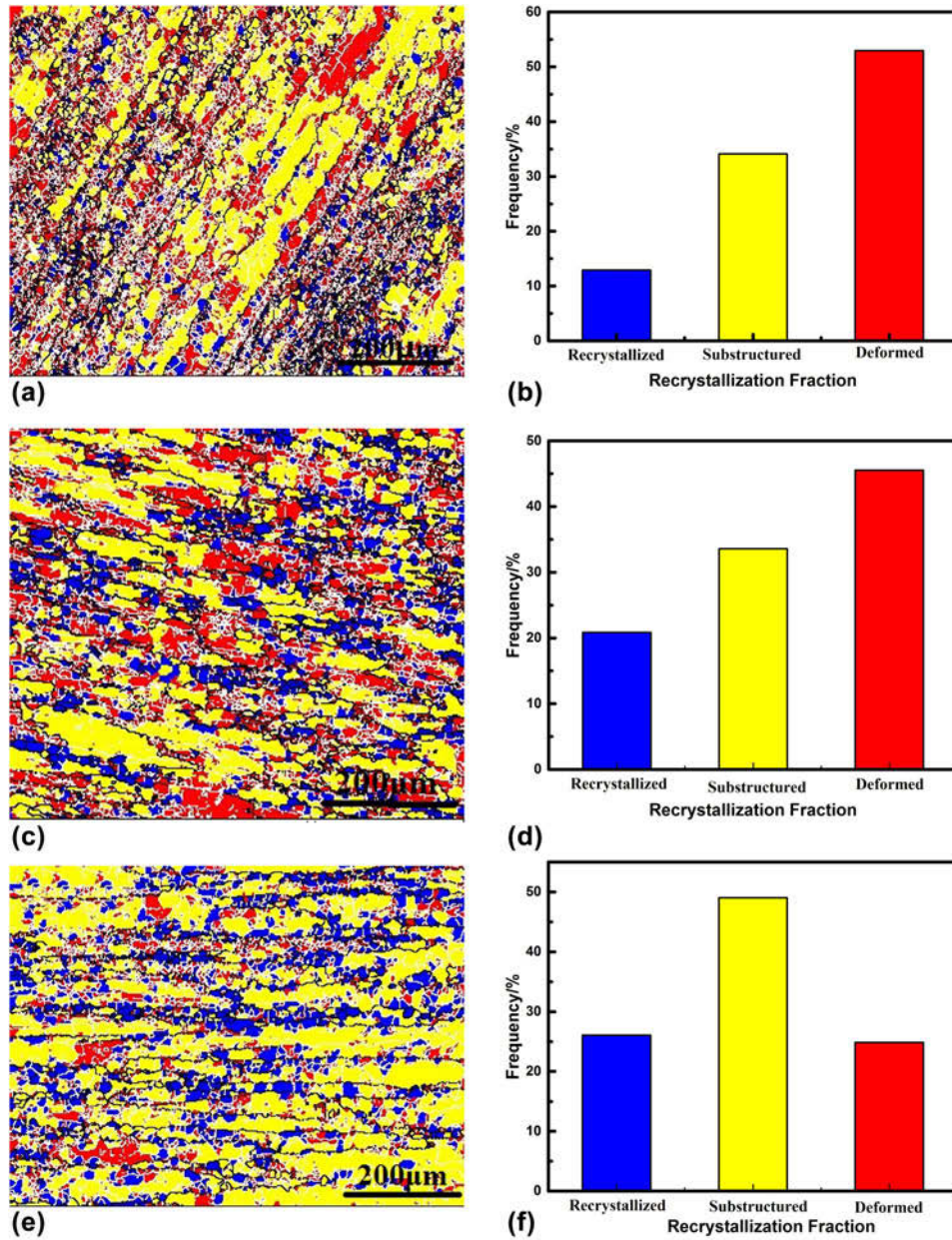
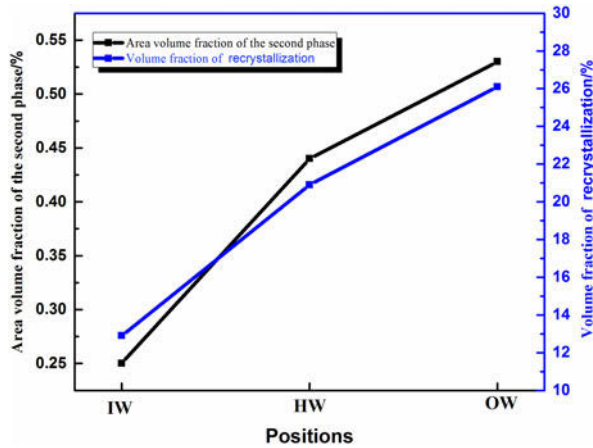


Figure 5: OIM images of aged high strength alloy pipes: (a) and (b) at the IW; (c) and (d) at the HW; (e) and (f) at the OW.

The degree of recrystallization of an aluminum alloy is related to the degree of deformation of the alloy [3, 4, 5]. The degree of deformation observed on the cross section of the aluminum alloy pipe as a result of reverse extrusion is not uniform. The larger the deformation, the higher the energy storage and the higher degree of recrystallization. As can be seen from Fig. 1, the IW and OW of the pipe exhibited greater deformation and a greater degree of recrystallization. Under the effects of alloy deformation process, the degree of recrystallization in the OW of the pipe is the highest, followed by the HW; the degree of recrystallization in the IW is the lowest. According to the formula [25],

$$\sigma_{gb} \cong \alpha_2 Gb(1 - f_{\text{Rex}}) \frac{1}{\delta} \quad (2)$$

where  $G$  is the shear modulus of alloy,  $b$  is the burgers vector,  $f_{\text{Rex}}$  is the volume fraction of recrystallization,  $\delta$  is the sub-grain size in non-recrystallized region, and  $\alpha_2$  is the constant. It can be seen from Fig. 6 that the volume fraction of recrystallization  $f_{\text{Rex}}$  of OW is lightly higher than the  $f_{\text{Rex}}$  of IW and OW. Thus, the strength and hardness of the OW of the alloy is lower than that of the HW. Recrystallization can reduce the strength and hardness of an alloy, but it can also improve the plasticity of the alloy, so the plasticity of the OW



**Figure 6:** The volume fraction of recrystallization and area volume fraction of the second phase of the IW, HW, and OW.

is higher than that of the IW, as shown in Fig. 1. In order to achieve more uniform pipe deformation during the process of directional extrusion, the bearing length of the extrusion die corresponding to the OW should be increased appropriately [26].

Under the combined action of  $\eta'$  phase precipitation and recrystallization in the alloy, the mechanical properties observed in the various regions of the cross section of the aluminum alloy pipe were substantially different. The factors contributing to the strength of the studied alloy can be divided into the following parts, as shown in the following formula [27]:

$$\sigma = \sigma_m + \sigma_{ss} + \sigma_p + \sigma_g \quad (3)$$

where  $\sigma_m$  is the strength of aluminum matrix,  $\sigma_{ss}$  is the effect of solution strengthening,  $\sigma_p$  is the strengthening effect by precipitation, and  $\sigma_g$  is the strengthening effect of grain structure and texture. However, precipitation strengthening still dominates in the present study. The strengthening effect of the  $\eta'$  phase is greater than that of recrystallization; thus, the HW had the highest hardness and strength. The second phase dispersion precipitation also improved the plasticity of the HW. Recrystallization to a large extent improves the plasticity of the OW and reduces its strength and hardness, but the strength and hardness of the OW of the pipe is still higher than that of the IW due to the precipitation of a large number of second phases.

## Conclusions

The effect of microstructure heterogeneity on the mechanical properties of high strength aluminum alloy thick-wall pipes was studied by optical microscopy, scanning electron microscopy, transmission electron microscopy, HRTEM, and electron

back scattered diffraction (EBSD). The following conclusions can be made:

- (1)  $\eta'$  phase is the main strengthening phase of the studied aluminum alloy. The content of Zn, Al, and Cu in the alloy affects the precipitation density and size of the phase. A large number of fine dispersed  $\eta'$  phase were precipitated in the HW, owing to the high contents of Al, Zn, and Cu. The content of Zn and Mg at the IW was the lowest, and less  $\eta'$  phase was precipitated at the IW. Therefore, the strength and hardness at the HW of the pipe was the highest, followed by the OW; the strength and hardness of the IW was the lowest.
- (2) Under the dual effects of the alloy deformation process, the degree of recrystallization at the OW of the pipe was the highest, followed by the HW. Recrystallization can reduce the strength and hardness of an alloy, but it can also improve the plasticity of the alloy; thus, the strength and hardness of the OW of the alloy was lower than that of the HW, while the plasticity of the OW was higher than that of IW.
- (3) Under the combined action of  $\eta'$  phase precipitation and recrystallization in the alloy, the mechanical properties of the aluminum alloy pipe exhibited substantial differences throughout the thickness of the pipe wall. The UTS and Vickers hardness first increased and then decreased from the IW to the OW; both were maximum at the HW. The maximum UTS and Vickers hardness were 630.5 MPa and 155.5 HV, respectively. However, El exhibited the opposite trend; the maximum El was 12.8% at the IW.

## Experimental materials and procedures

In order to enhance the strength of the 7050 aluminum alloy, the material employed in this paper was an Al-Zn-Mg-Cu alloy prepared by increasing the Zn content of a 7050 aluminum alloy [21, 28]. High strength aluminum alloy pipes with a wall thickness of 20 mm and an internal diameter of 110 mm were manufactured by reverse hot extrusion under an extrusion ratio of 8.4. Age hardening treatment of the extruded pipes included two-stage solution treatment at 475 °C for 2 h and 495 °C for 1 h, followed by water quenching and two-step aging. The aging process was carried out by initially exposing the solution-treated specimen to room temperature ( $25 \pm 5$  °C) for 6.5 h and then 136 °C for 16 h. In order to study the through-wall thickness heterogeneity of the pipes, three regions of the pipe wall were defined: near the IW, near the OW, and the HW. A series of microstructure observations and tests of properties were



carried out on the three regions. The chemical compositions of the three regions of the primary high strength alloy hollow ingot and the thick-wall pipe were measured by a direct-reading spectrometer. Grain morphology and recrystallization of the extruded pipes were examined by optical microscopy (OM) with samples cut from the IW, HW, and OW, parallel to the direction of extrusion. Samples for OM were prepared by mechanical polish and chemical etch (Keller reagent: 2.5% nitric acid, 1.5% hydrochloric acid, 1% hydrofluoric acid, and 95% aqua destillata). The precipitates in the aged pipes were characterized using a Titan G2 60-300 (FEI Corporation, Hillsborough, Oregon) transmission electron microscope (TEM) operated at 200 kV. Foils 3 mm in diameter and 80 μm in thickness were prepared and twin-jet electropolished in a solution of 25% nitric acid and 75% methanol at a temperature of −30 °C and a voltage of 13 V. The area volume fractions were statistically analyzed over a number of BF images using image analysis software [Image-pro plus (Image Processing Software) Media Cybernetics Corporation, Maryland]. Samples for EBSD taken from the pipe were prepared by mechanical polishing and then were vibratory polished for 2 h. EBSD was performed on an FEI NOVA NanoSEM (Philips Corporation, Holland) equipped with a field emission gun (FEG) at an operation voltage of 20 kV. A step size of 2 μm was used for the beam scanning. The obtained patterns were post-processed by CHANNEL 5-Oxford Instruments software, Oxford Instrument Technology (Shanghai) Co., Ltd. Oxford, U.K.

The Vickers hardness of the samples was measured using a Vickers hardness tester (model HVS-1000, Shanghai Unier Test Equipment Co., Ltd. Shanghai, China) at a load of 0.5 kg with a holding time of 15 s; each hardness value was determined as the average of six indentations. Uniaxial tensile tests were performed at room temperature by an Instron3369 [Intenter (Shanghai) Test Equipment Trade Co., Ltd., Boston] at a strain rate of  $1 \times 10^{-3} \text{ s}^{-1}$ . The sampling method for tensile tests is shown in Fig. 7. The ED and RD in Fig. 7

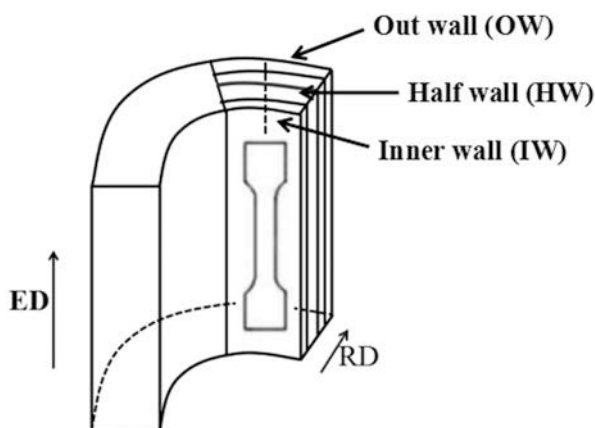


**Figure 7:** Scheme of sampling method for tensile tests.

represent the extrusion direction and radial direction of the pipe, respectively. The gauge length, width, and wall thickness of the tensile samples were 35 mm, 6 mm, and 1.5 mm, respectively. At least three samples were examined to acquire average values of UTS and El.

## Acknowledgments

This study was supported by the National Natural Science Foundation of China (No. 51274245).

## References

1. **C. Mondal, A.K. Mukhopadhyay, T. Raghu, and V.K. Varma:** Tensile properties of peak aged 7055 aluminum alloy extrusions. *Mater. Sci. Eng., A* **454**, 673 (2007).
2. **T. Dursun and C. Soutis:** Recent developments in advanced aircraft aluminium alloy. *Mater. Des.* **56**, 862 (2014).
3. **R. Su, Y. Qu, J. You, and R. Li:** Study on a new retrogression and re-aging treatment of spray formed Al–Zn–Mg–Cu alloy. *J. Mater. Res.* **31**, 573 (2106).
4. **Y.C. Lin, Z.W. Wang, D.G. He, Y. Zhou, M-S. Chen, M-H. Huang, and J-L. Zhang:** Effects of pre-treatments on precipitate microstructures and creep-rupture behavior of an Al–Zn–Mg–Cu alloy. *J. Mater. Res.* **31**, 1286 (2016).
5. **D. Feng, G. Wang, H. Chen, and X. Zhang:** The effect of grain size inhomogeneity of ingot on dynamic softening behavior and processing map of Al–8Zn–2Mg–2Cu alloy. *Met. Mater. Int.* **24**, 195 (2018).
6. **F. Cong, G. Zhao, F. Jiang, N. Tian, and R. Li:** Effect of homogenization treatment on microstructure and mechanical properties of DC cast 7X50 aluminum alloy. *Trans. Nonferrous Met. Soc.* **25**, 1027 (2015).
7. **K. Chen, H. Liu, Z. Zhang, S. Li, and R. Todd:** The improvement of constituent dissolution and mechanical properties of 7055 aluminum alloy by stepped heat treatments. *J. Mater. Process. Technol.* **142**, 190 (2003).
8. **Z. Huda and P. Edi:** Materials selection in design of structures and engines of supersonic aircrafts: A review. *Mater. Des.* **46**, 552 (2013).
9. **J. Chen, L. Zhen, W. Shao, S. Dai, and Y. Cui:** Through-thickness texture gradient in AA 7055 aluminum alloy. *Mater. Lett.* **62**, 88 (2012).
10. **S. Liu, Y. Zhang, W. Liu, Y. Den, and X. Zhang:** Effect of step-quenching on microstructure of aluminum alloy 7055. *Trans. Nonferrous Met. Soc.* **20**, 1 (2010).
11. **S. Liu, C. Li, S. Han, Y. Den, and X. Zhang:** Effect of natural aging on quench-induced inhomogeneity of microstructure and hardness in high strength 7055 aluminum alloy. *J. Alloys Compd.* **625**, 34 (2015).

12. **H. She, D. Shu, J. Wang, and B. Sun:** Influence of multi-microstructural alterations on tensile property inhomogeneity of 7055 aluminum alloy medium thick plate. *Mater. Char.* **113**, 189 (2016).
13. **M. Prime and M. Hill:** Residual stress, stress relief, and inhomogeneity in aluminum plate. *Scripta Mater.* **46**, 77 (2002).
14. **L. Yan, J. Shen, Z. Li, and J. Li:** Effect of deformation temperature on microstructure and mechanical properties of 7055 aluminum alloy after heat treatment. *Trans. Nonferrous Met. Soc.* **23**, 625 (2013).
15. **S. Liu, X. Zhang, M. Chen, and J. You:** Influence of aging on quench sensitivity effect of 7055 aluminum alloy. *Trans. Nonferrous Met. Soc.* **59**, 53 (2008).
16. **C. Li, X. Zhang, S. Han, S. Liu, and Y. Den:** Effect of aging on quench-induced inhomogeneity of 7085 aluminum alloy thick plate. *Chin. J. Nonferrous Met.* **46**, 2824 (2016).
17. **W. Gu, J. Li, and Y. Wang:** Effect of grain size and Taylor factor on the transverse mechanical properties of 7050 aluminium alloy extrusion profile after over-aging. *Acta Metall. Sin.* **52**, 51 (2016).
18. **J. Williams:** The effect of material inhomogeneity on the creep deformation of a thick walled pipe. *Int. J. Pressure Vessels Piping* **11**, 1 (1983).
19. **M. Li, Y. Yang, Z. Feng, B. Huang, X. Luo, X. Lou, J. Lou, and J. Ru:** Precipitation sequence of  $\eta$  phase along low-angle grain boundaries in Al–Zn–Mg–Cu alloy during artificial aging. *Trans. Nonferrous Met. Soc.* **24**, 2061 (2014).
20. **X. Li, V. Hansen, J. Gjønnnes, and L. Wallenberg:** HREM study and structure modeling of the  $\eta'$  phase, the hardening precipitates in commercial Al–Zn–Mg alloy. *Acta Mater.* **47**, 2651 (1999).
21. **H. She, D. Shu, W. Chu, J. Wang, and B. Sun:** Microstructural aspects of second phases in as-cast and homogenized 7055 aluminum alloy with different impurity contents. *Metall. Mater. Trans. A* **44**, 3504 (2013).
22. **T. Marlaud, A. Deschamps, F. Bley, W. Lefebvre, and B. Barouxa:** Influence of alloy composition and heat treatment on precipitate composition in Al–Zn–Mg–Cu alloys. *Acta Mater.* **58**, 248 (2010).
23. **A. Lakshminarayanan and V. Balasubramanian:** Process parameters optimization for friction stir welding of RDE-40 aluminium alloy using Taguchi technique. *Trans. Nonferrous Met. Soc.* **18**, 548 (2008).
24. **Y. Liu, D. Jiang, B. Li, T. Ying, and J. Hu:** Heating aging behavior of Al–8.35Zn–2.5Mg–2.25Cu alloy. *Mater. Des.* **60**, 116 (2014).
25. **D. Feng, X. Zhang, S. Liu, Z. Wu, Y. Guo, and W. Yu:** Inhomogeneity of microstructure and properties of 7A55 aluminium alloy thick plate. *J. Cent. South Univ.* **46**, 2824 (2015).
26. **J. Lee, B. Kim, and C. Kang:** Effects of chamber shapes of porthole die on elastic deformation and extrusion process in condenser tube extrusion. *Mater. Des.* **26**, 327 (2005).
27. **M. Starink and S. Wang:** A model for the yield strength of overaged Al–Zn–Mg–Cu alloys. *Acta Mater.* **51**, 5131 (2003).
28. **Y. Liu, D. Jiang, W. Xie, J. Hu, and B. Ma:** Solidification phases and their evolution during homogenization of a DC cast Al–8.35Zn–2.5Mg–2.25Cu alloy. *Mater. Char.* **93**, 173 (2014).